Chapter 4

A Single ended Traveling Wave based DC fault localization for MTDC grid

4.1 General

This chapter proposes a single ended TW based MTDC fault localization scheme which uses AT of the first incident TW extracted from high frequency sampled and derived low sampling frequency (downsampled and filtered) aerial mode voltage signal at the DC terminal, which is applicable for localizing pole-to-pole and pole-to-earth fault in MTDC grid. It also eliminates the need for identifying TW reflection from the fault point, which is traditionally a challenging task for conventional single ended TW based fault localization scheme.

4.2 Proposed single ended TW based fault localization scheme

This novel fault localization scheme utilizes the frequency-domain characteristics of TWs. It stands out as the first method to harness these properties and, notably, eliminates the necessity for communication protocols. It solely relies on the frequency and damping factor properties of the only first incident TW generated by a fault, thus circumventing the

challenges posed by detecting the timing of second TW. This scheme also boasts several notable characteristics such as sensitivity to high-resistance faults and ensuring precise localization of faults. Furthermore, this method is distinguished by its exceptional fault location accuracy and its ability to operate independently of the grid's configuration.

A DC fault triggers the initiation of voltage traveling waves (v_{TW}) and current traveling waves (i_{TW}) that propagate outward from the fault location in two directions towards the terminals of the line (or cable). In the proposed scheme, the damping factor and frequency content of i_{TW} is used to locate DC fault accurately.

4.2.1 Complex frequency content of the TW

The subsequent equations are employed to provide a mathematical representation of voltage traveling waves (V_{TW}) and current traveling waves (I_{TW}) at a distance X in the frequency domain [125]:

$$\frac{dV_{TW}(\omega)}{dX} = -Z_s(\omega)I_{TW}(\omega) \tag{4.1}$$

$$\frac{dI_{TW}(\omega)}{dX} = -Y_s(\omega)V_{TW}(\omega) \tag{4.2}$$

Where, V_{TW} and I_{TW} are implicitly reliant on the angular frequency ω. V_{TW} and I_{TW} are, respectively, the Fourier transforms of voltages and currents at specific ω values within the trajectory of the Fourier integral [125]. Differentiating equation 4.2 leads to the subsequent decoupled depiction of I_{TW}:

$$\frac{d^2I_{TW}(\omega)}{dX^2} = -Y_s(\omega)Z_s(\omega)I_{TW}(\omega) \tag{4.3}$$

Solving 4.3 for I_{TW} at a distance of X [126],

$$I_{TW}(\omega, X) = I_i e^{-\gamma(\omega)X} + I_r e^{\gamma(\omega)X} \tag{4.4}$$

The propagation constant γ, is given by

$$\gamma(\omega, X) = \alpha + j\beta = \sqrt{Z_s(\omega)Y_s(\omega)} \tag{4.5}$$

The equations mentioned above reveals that the frequency dependency of traveling waves (TW) emerges from $Z_s(\omega)Y_s(\omega)$. For single-conductor lines, $Z_s = R_l + j\omega L_l$ and $Y_s = G_l + j\omega C_l$. The real component of γ represents the attenuation constant (α), while the imaginary part signifies the phase constant (β). α is a parameter subject to frequency

variations and stands as the primary factor behind TW attenuation. The TW attenuation factor (α) can be disintegrated into the following four loss components [127]:

1. Skin-effect loss (α_S)
2. Dielectric loss (α_D)
3. Conductivity of dielectric loss (α_G)
4. Radiation loss (α_R).

α_G and α_R have a negligible impact on the overall value of α and can therefore be disregarded [127]. Conversely, α_S, which primarily accounts for TW attenuation at lower frequencies, is reliant on R. This parameter is directly proportional to the square root of the frequency of a component and is represented as follows [127]:

$$\alpha_S = \frac{R}{2Z_c} = \frac{1}{2Z_c}\sqrt{\frac{\pi\mu f}{\sigma}} \tag{4.6}$$

Where, σ denotes the conductivity of the conductor, μ represents the permeability of the conductor, f stands for the frequency of a specific TW component, and Z_c signifies the characteristic impedance of the line/cable, which can be expressed as:

$$Z_c = \sqrt{\frac{R + j\omega L}{G + j\omega C}} \tag{4.7}$$

On contrary, α_d is the dominant component of the α at higher frequency. This value relies on C and is directly proportional to the frequency of a specific component. It can be expressed as [127]:

$$\alpha_D = \frac{\omega C Z_c tan\delta}{2} = \frac{\pi\sqrt{\epsilon_r}tan\delta}{2} f \tag{4.8}$$

In equation 4.8, $tan(\delta)$ stands for the dielectric dissipation factor and ϵ_r denotes the relative dielectric constant. It becomes apparent that α_s and α_D are closely tied to the frequency f components and that's why the damping factor coefficient depends on the sampling frequency selection. Moreover, given that α is linked to per-unit length quantities in (4.5), the cumulative attenuation of traveling waves for each frequency component increases as the traveled distance of the waves increases. Moreover, the accurate transient behavior of the overhead transmission line (OHTL) and cable demonstrates multiple complex frequency component of the fault or disturbance induced TW, which is known as the

TW dispersion effect [118]. It explains the idea of different complex frequency component of the TW propagating at different TW velocity, which depends on the frequency dependent line parameters and sampling frequency measurement selection. It can be infer that the traveling wave velocity and fault induced TW arrival time (TWAT) is also dependent on the selection of sampling frequency measurement.

4.2.2 Operating principle of proposed scheme

Consider a DC fault F_1 at a distance of xl_{AB} from DC bus A, in DC link of length l_{AB} in a simple two terminal HVDC link as shown in Fig. 4.1.

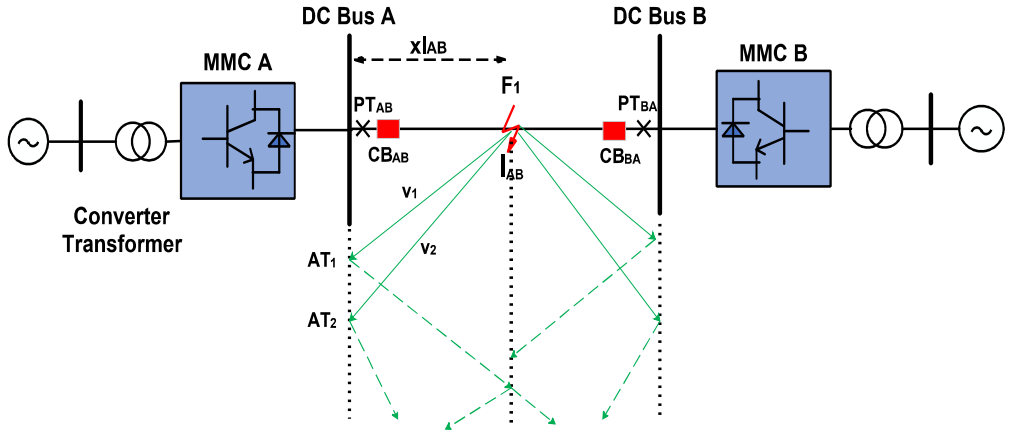

Figure 4.1: Simple two terminal HVDC transmission system.

The TW lattice diagram is also shown in Fig. 4.1, where the two distinctive TW with two different velocity (corresponding to respective sampling frequency measurement selection) travels from DC fault location to DC terminal A at AT_1 (high sampling frequency) and AT_2 (low sampling frequency) respectively. Mathematically, the TWATs at DC terminal A is given by -

$$AT_1 = t_0 + xl_{AB}/v_1 \tag{4.9}$$

$$AT_2 = t_0 + xl_{AB}/v_2 \tag{4.10}$$

Where, t_0 is the fault inception time and v_1, v_2 are the TW velocity corresponding to sampling frequency f_1 (higher) and f_2 (lower) respectively. Subtracting (4.9) from (4.10),

$$AT_2 - AT_1 = xl_{AB} * (\frac{1}{v_2} - \frac{1}{v_1}) = xl_{AB} * (\frac{v_1 - v_2}{v_1 * v_2}) = xl_{AB} * VF \tag{4.11}$$

Where, VF is the TW velocity factor which is predetermined for selected set of sampling frequency measurement f_1 (higher) and f_2 (lower). The calculated DC fault location is given by -

$$xl_{AB} = \frac{|AT_1 - AT_2|}{VF} \tag{4.12}$$

Moreover, the fault location error (FLE) for the proposed fault localization scheme is mathematically given as -

$$FLE = \frac{|AFL - CFL|}{l} * 100 \tag{4.13}$$

Where, AFL and CFL are the actual and calculated fault location of the DC fault in the MTDC grid.

4.2.3 Proposed TWAT extraction technique for low and high sampling frequency measurement

Prior to calculating the arrival time of TW, it is essential to negate the influence of mutual coupling effect on TW. This can be achieved by applying the modal transformation equation depicted as follows [30]:

$$\begin{bmatrix} V_{m0} \\ V_{m1} \end{bmatrix} = \frac{1}{\sqrt{2}} \begin{bmatrix} 1 & 1 \\ 1 & -1 \end{bmatrix}^{-1} \begin{bmatrix} V_p \\ V_n \end{bmatrix} \tag{4.14}$$

Here, V_{m0} and V_{m1} denote the for mode-0 and mode-1 voltage respectively. Meanwhile, V_p and V_n represent the current in the positive and negative DC poles respectively. As evident from equation (4.14), it is clear that V_{m0} remains at zero during pole-to-pole (PP) faults and steady-state operation. However, it takes a non-zero value during positive-pole-to-ground (PPG) and negative-pole-to-ground (NPG) faults. On the other hand, V_{m1} holds a non-zero value for PP, PPG, as well as NPG faults. Hence, the mode-1 voltage (V_{m1}) is selected as the decoupled mode voltage signal for extracting AT information of the voltage TW.

As described in Section 4.2.1, the damping factor part of the each complex frequency component of the TW increases as the distance traveled by the TW increases. Mathematically, the band-limited signals can be expressed as a summation of damped sinusoidal signals, depicted as follows

$$V_{m1}(t) = \sum_{m=1}^{M} B_m e^{-\alpha_m t} \sin(\omega_m t + \theta_m) \tag{4.15}$$

Where signal $V_{m1}(t)$ is the weighted sum of M number of sinusoids in a time period T with residue $B_m \angle \theta_m$. And where α_m (s^{-1}) and ω_m (rad/s) are the damping factor (real part) and angular frequency (imaginary part) of the m^{th} complex frequency ($\alpha_m \pm j\omega_m$) respectively. To extract complex frequency parameter and residue in 4.15, matrix pencil method (MPM), estimation of signal parameters via rotational invariant techniques (ESPIRIT), and Prony method can be used. Out of this, MPM is typically favored over alternative parameter estimation methods, particularly in situations involving noise [128, 129].

A compact window of fixed size is moved along the time axis, and the MPM is applied to signal samples within the window to estimate signal parameters, which is known as Sliding MPM (SMPM). In Fig. 4.2(b), SMPM and Short-Time Discrete Fourier Transform (STDFT) are utilized to reconstruct a positive pulse signal shown in Fig. 4.2(a) for the same number of sinusoidal terms. Notably, SMPM outperforms STDFT due to its utilization of two degrees of freedom - damping factors and sinusoids - as opposed to STDFT's reliance solely on sinusoids for signal reconstruction.

For each signal sample within the sliding window, MPM is applied, resulting in time-indexed complex frequencies as the window moves. Illustrated in 4.2(c), the damping factor (α) starts close to zero (with possible variations due to measurement noise) before the pulse (traveling wave) arrives. As the pulse enters from the right side of the window, SMPM detects a positive damping factor value. During the window's advancement, the damping factor gradually decreases to zero when the pulse is positioned at the center of window. Further movement of the window causes the damping factor to decrease even more, becoming negative as the pulse moves towards the left side of the window, as depicted in 4.2(c).

This principle can be applied to detect the arrival time of fault-induced traveling waves. Mathematically, this concept can be expressed as follows -

$$\alpha_m = 0, \forall m \rightarrow AT = t_0 + T_l/2 \tag{4.16}$$

Where α_m, t_0, and T_l are the damping factor, location of the sliding window, and sliding window length respectively. Based on the principle explained in earlier, the arrival time of the fault-induced TW is extracted using SMPM. The formulation of SMPM involves forming a Hankel matrix $X_{(M-1)(L+1)}$ using the samples in M sized sliding window

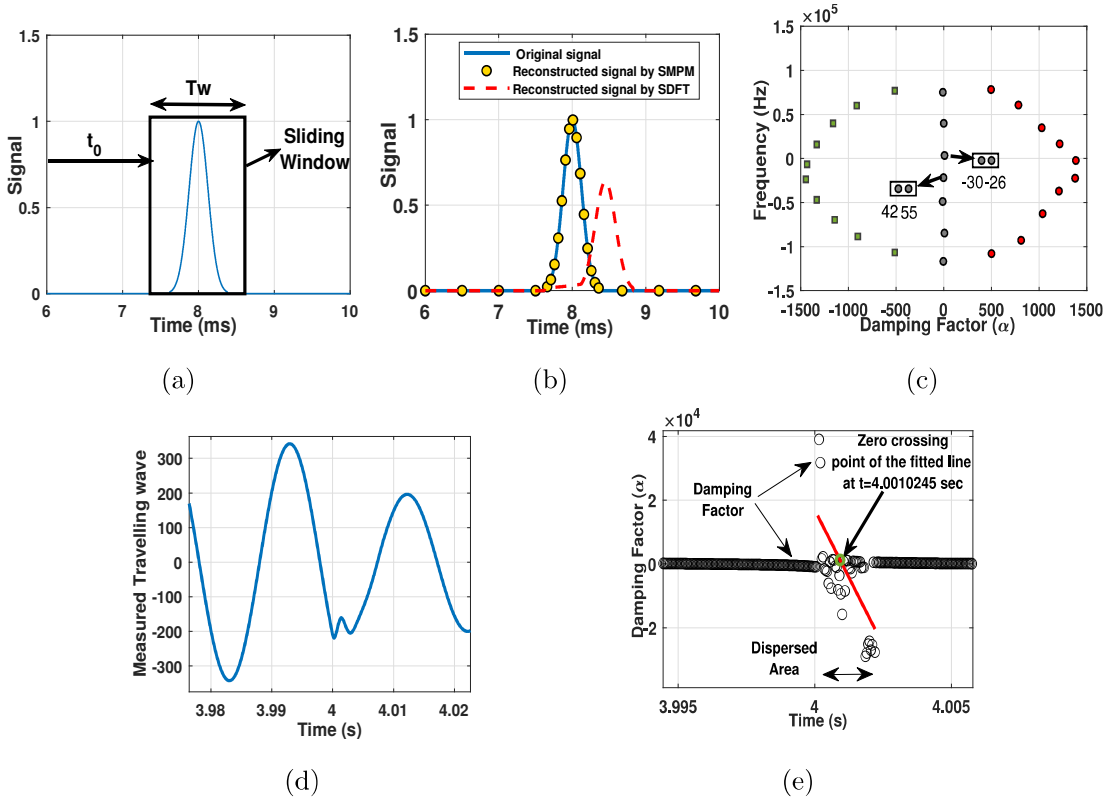

Figure 4.2: (a) Pulse signal. (b)Reconstructed signal by SMPM and STDFT, (c) Complex frequency extracted by SMPM for the pulse signal, (d) Fault-induced TW, (e) Time index damping factor diagram with linear regression to detect zero crossing point

is shown below in (4.17)-

$$X = \begin{pmatrix} V_{m1}(1) & V_{m1}(2)\cdots\cdots & V_{m1}(L+1) \\ V_{m1}(2) & V_{m1}(3)\cdots\cdots & V_{m1}(L+2) \\ \vdots & \vdots & \vdots \\ V_{m1}(N-L) & V_{m1}(N-L+1)\cdots & V_{m1}(N) \end{pmatrix} \tag{4.17}$$

Here, $V_{m1}(.)$, M and L represents mode-1 signal samples, number of samples, and pencil parameters respectively. It is recommended that the pencil parameters L falls within the range of M/3 to M/2for effective noise filtering [130]. Following this, a singular value decomposition (SVD) will be executed on the matrix X, as outlined below -

$$X = R\Sigma S^H \tag{4.18}$$

Here $(.)^H$ represents the complex conjugate of the matrix, whereas R and S are the unitary matrices having their elements as eigenvectors of XX^H and X^HX respectively.

Meanwhile, Σ takes the form of a diagonal matrix containing the singular or eigenvalues of X. Subsequently, the most significant or dominant singular value from the matrix Σ is filtered out as -

$$\sigma_{ds} = 10^{-p}\sigma_{sd\max} \tag{4.19}$$

Here, σ_{ds} represents the dominant singular value, $\sigma_{sd\max}$ signifies the maximum value among the dominant singular values within Σ, and p is referred as the filtering parameter [130]. Subsequently, the matrix Σ is compressed to form Σ', conserving its column elements corresponding to the dominant singular value. Similarly, a fresh condensed matrix S', derived from matrix S, is constructed [130]. Utilizing Σ' and S', a new matrices are established -

$$\begin{aligned} X_1 &= R\Sigma' S_1'^H \\ X_2 &= R\Sigma' S_2'^H \end{aligned} \tag{4.20}$$

Where S_1 and S_2 are formed by eliminating the last and first rows of the S' matrix. Another matrix $X_1^+X_2$ ($(.)^+$ represent pseudoinverse) is formulated, whose eigenvalues can be used to find the complex frequencies of the windowed signal as follows [130] -

$$\lambda_m = e^{(-\alpha_m \pm j\omega_m)T_s}, \forall m = 1, 2, 3.....n \tag{4.21}$$

Here, λ_m symbolizes the eigenvalue of matrix $X_1^+X_2$, and T_s represents the sampling time interval. The eigenvalue parameter λ_m can be employed to determine time-indexed complex frequencies using the subsequent equation -

$$\alpha_m(t) \mp j\omega_m(t) = -\ln(\lambda_m)/T_s, \forall m = 1, 2, 3...n \tag{4.22}$$

Equations (4.17)-(4.22) are reiterated for the signal samples inside the sliding window. To illustrate its performance, SMPM with a window width of $T_w = 0.150\ ms$ is applied to the noise contaminated signal, as depicted in Fig. 4.2(d). The arrival time of the TW can be determined as 4.0010245 s using SMPM, as illustrated in Fig. 4.2(e). It's noteworthy that the TW arrival time estimated via SMPM closely aligns with the zero damping factor location. But for more accurate TW arrival time estimation, zero-crossing point of damping factors need to be calculated with dispersed damping factors as independent variables and time as the independent variable with linear regression equation as shown below -

$$\alpha_m(t) = c_0 + c_1 t + \varepsilon_m(t), \forall t \in (t_a, t_b), \forall m \tag{4.23}$$

In this equation, $\alpha_m(t)$ represents the time-dependent damping factor, while t_a and t_b denote the initial and final time stamps for the dispersed region of the time-dependent damping factors, as depicted in Fig. 4.2(e). c_0 (a constant term) and c_1 (a slope coefficient) constitute the linear regression coefficients, and $\varepsilon_m(t)$ stands for the error in linear regression equation at time t. (4.23) can be reformulated in matrix notation, as illustrated below -

$$\alpha = tc + \varepsilon \tag{4.24}$$

Where $\alpha = [\alpha_m(t_1), ..., \alpha_m(t_2)]^T$ is the time-stamped damping factor matrix, $c = [c_0, c_1]^T$ is the linear regression coefficient vector, $\varepsilon = [\varepsilon(t_1), ..., \varepsilon(t_2)]^T$ is the error vector, and $t = \begin{bmatrix} 1.....1 \\ t_1.....t_2 \end{bmatrix}^T$ is the matrix of time or independent variable in this case. The regression coefficient for (4.24) can be calculated by solving the following equations -

$$\min_{c_0,c_1}(\alpha - tc) \tag{4.25}$$

The solution for (4.25) will be -

$$\hat{c} = (t^T t)^{-1} t^T \alpha \tag{4.26}$$

Here $\hat{c} = [\hat{c}_0, \hat{c}_1]^T$ is the estimated regression coefficient vector of (4.26) and $(.)^T$ represents the transposition of matrix. TW arrival time can be found by estimating the zero-crossing point of damping factor by solving the equation $\hat{c}_0 + \hat{c}_1 t = 0$, which is -

$$TWAT = -\frac{\hat{c}_0}{\hat{c}_1} \tag{4.27}$$

Where TWAT is the traveling arrival time estimation and the TW arrival time of fault-induced aerial wave is estimated very accurately as evident from Fig. 4.2(e).

4.3 Test MTDC transmission system

To evaluate the effectiveness of proposed fault localization method, a test meshed MMC converter based MTDC transmission system is utilized, as shown in Fig. 4.3. The configuration comprises two half-bridge MMC converters (MMC 1 and MMC 3) interconnecting an offshore wind farm. These converters feed power into an onshore AC grid, which is connected to two additional half-bridge MMC converters (MMC 2 and MMC 4). This

test MMC-MTDC system is modeled in a symmetrical monopolar configuration, with a DC voltage of ± 320 kV. The MTDC grid has a 200 km DC link (L_{34}), a 150 km DC link (L_{12}), a 250 km DC link (L_{32}), and two 100 km DC links (L_{13} and L_{24}). At the terminals of each DC link, a DC bus reactor with an inductance of 10 mH and a hybrid DC Circuit Breaker (HDCCB) are integrated. More comprehensive parameters of the MMC converters and the AC/DC grid system are outlined in Table 4.1 [98].

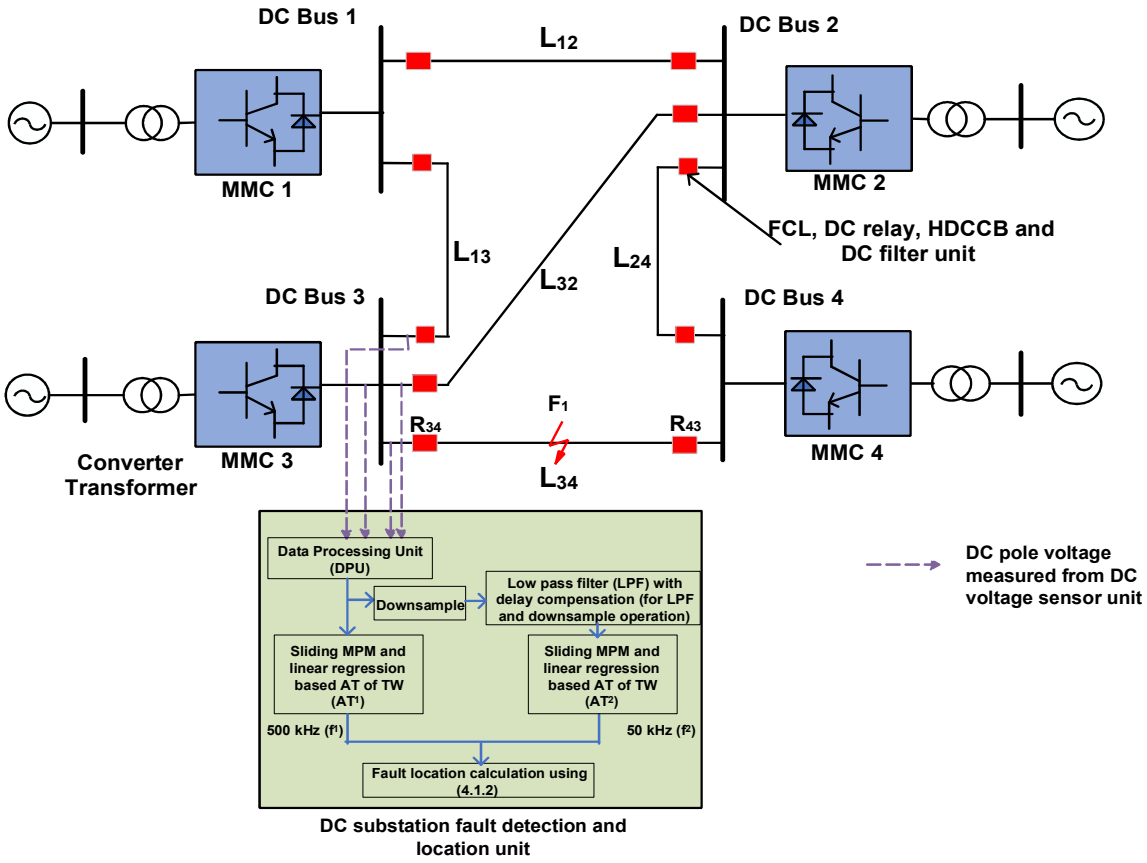

Figure 4.3: Test MTDC transmission system.

The DC substation fault location unit comprises of data processing unit (DPU), which collects measured DC pole voltage from electrical potential transducers (EPTs) installed at the DC terminals using high sampling frequency measurement (50 kHz). The pre-processing of relaying input signals are performed in local DPU unit using (4.14). In next step, the proposed TWAT estimation technique is used to determine fault induced TWAT (AT_1) at local DC terminal ends of transmission line for high sampling frequency (f_1) measurement data. The same high frequency sampled mode-1 voltage data is passed through downsample and 2^{nd} order Butterworth low pass filter (LPF), with appropriate

low frequency cutoff (f_2), and delay compensation logic for downsampler and LPF operation. In parallel, arrival time (AT_2) of the fault induced TW for low frequency mode-1 DC voltage signal is estimated using sliding matrix pencil method. In the final stage, (4.12) is used to calculate DC fault location in the MTDC grid as shown in Fig. 4.3.

Table 4.1: MMC converter and AC/DC grid parameters

Converter and grid parameters	Converter 1,2,3	Converter 4
Rated power (MVA)	900	1200
AC grid voltage (kV)	400	400
DC grid voltage (kV)	± 320	± 320
AC converter voltage (kV)	380	380
AC grid reactance (Ω)	17.7	13.4
AC grid resistance (Ω)	1.77	1.34
Arm capacitance (μF)	29.3	39
Arm reactor (mH)	84.8	63.6
Arm resistance (Ω)	0.885	0.67
Bus filter reactor (mH)	10	10

4.4 Simulation Results

The PSCAD/EMTDC is used for the purpose of simulating the MMC-MTDC test system depicted in Fig. 4.3. The half bridge MMC converter is modeled in the simulation tool using a continuous equivalent model of the MMC with blocking and de-blocking capability. Additionally, the cables are represented through a frequency-dependent (phase) model, specifically designed to accurately emulate the transient behavior of the meshed MMC-MTDC transmission system.

The speed at which traveling waves propagate along the DC cable im test MTDC grid is measured as 179 km/ms (v_1) and 155 km/ms (v_2) for 500 kHz (f_1) and 50 kHz (f_2) sampling frequency selection respectively, which is calculated by simulating a fault at known location and transient (TWAT) measurements within the MTDC system. In order to protect the MMC converter unit, the internal overcurrent and overvoltage protection

mechanism triggers blocking signals for the IGBTs. Throughout the simulation scenarios in the following study, a time step of 2 μs (equivalent to a sampling frequency of 500 kHz) and signal to noise ratio (SNR) of 40 dB is adopted, unless stated otherwise. The predefined threshold (ζ) for the test system is identified as $\pm 1 \times 10^5$ and $\pm 1 \times 10^4$ for 500 kHz and 50 kHz sampling frequency measurement selection respectively. The threshold value is determined empirically by simulating a fault scenario in a DC cable L_{34} with a fault resistance of 200 Ω (highest), positioned at a distance of 195 km (the farthest distance) from DC substation 3.

4.4.1 Impact of DC fault location

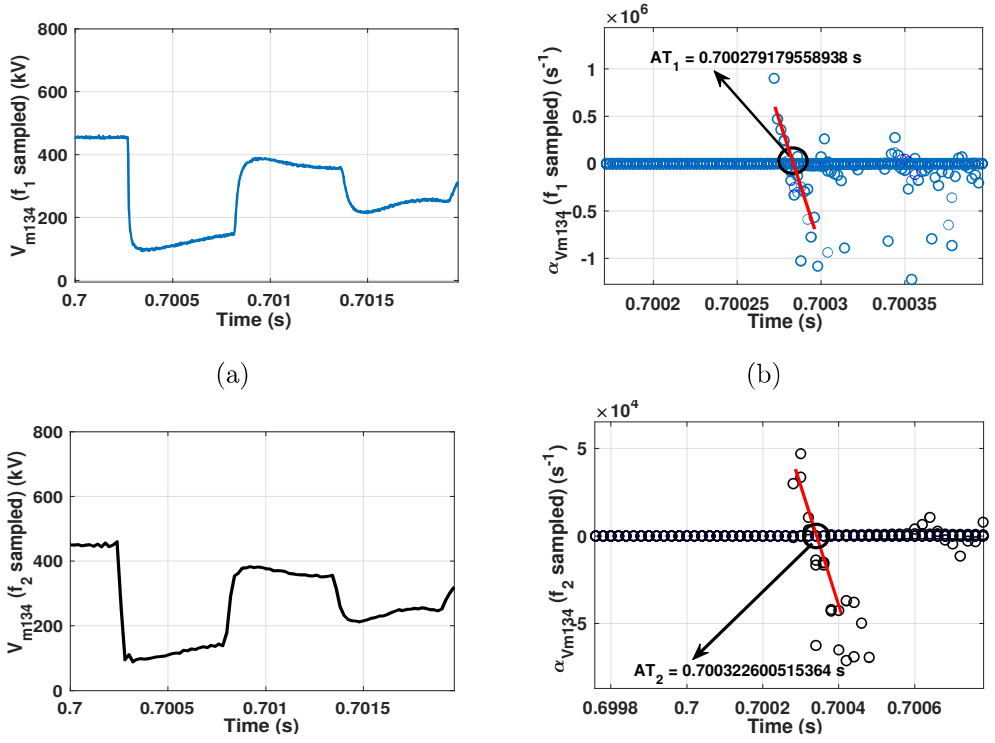

Figure 4.4: (a) Mode-1 DC voltage at DC terminal 3 with 500 kHz sampling frequency, (b) AT of the fault induced TW at DC terminal 3 for 500 kHz sampling frequency, (c) Mode-1 DC voltage at DC terminal 3 with 50 kHz downsampled frequency, (d) AT of the fault induced TW at DC terminal 3 for 50 kHz sampling frequency.

To study the impact of DC fault location on the proposed DC fault localization scheme, a 0.1 Ω positive pole to ground (PPG) DC fault resistance is simulated at 50

km distance from DC terminal 3 at 0.7 s in test MTDC transmission system. The proposed SMPM based TWAT estimation technique is used to extract AT of the TW as 0.700279179559 s and 0.7003226005154 s for the 500 kHz and 50 kHz sampling frequency respectively as shown from Fig. 4.4.(b) and (d).

The velocity factor for the DC cable L_{34} in the test MTDC transmission system, with reference to (4.11), comes out to be -

$$V.F. = \frac{v_2 - v_1}{v_2 \times v_1} = \frac{179 - 155}{179 \times 155} = 8.65 \times 10^{-4} ms/km$$

As per (4.12), the calculated fault location estimated by the proposed DC fault localization scheme is given by -

$$CFL = \frac{|AT_2 - AT_1|}{VF} = \frac{|0.7003226005154s - 0.700279179559s|}{8.65 \times 10^{-4} ms/km} = 50.203km$$

Table 4.2: Impact of fault location on proposed TW based fault localization scheme

Fault location (km)	AT of TW at DC terminal 3 (500 kHz), AT_1 (s)	AT of TW at DC terminal 3 (50 kHz), AT_2 (s)	($\|AT_1 - AT_2\|$) (μs)	Velocity Factor ($\mu s/km$)	CFL (km)	FLE (%)
1	0.700005588486	0.700007263804	1.68	1.937	0.4685	1.15
15	0.700083838420	0.700096780231	12.94	0.865	14.95	0.025
40	0.700223604372	0.700258085944	34.482	0.865	39.86	0.07
100	0.700558504183	0.700645146259	86.642	0.865	100.16	0.08
130	0.700726496550	0.700838713073	112.12	0.865	129.61	0.195
195	0.701089408139	0.701259035201	169.627	0.865	196.1	0.55

Similarly, the performance of proposed DC fault localization scheme is validated against different fault location on DC cable L_{34} in test MTDC grid and its performance is tabulated in Table 4.2. As evident from Table 4.2, the maximum FLE for the proposed DC fault localization scheme is 0.55 % out of all fault scenarios. The accuracy of proposed fault localization scheme depends on the selection of sampling frequency measurement (f_1 and f_2), which decides the velocity factor of the proposed scheme. If the difference

between f_1 and f_2 will be larger, then the accuracy of proposed scheme could be further improved.

4.4.2 Impact of fault resistance

To analyze the impact of fault resistance on the performance of proposed TW based fault localization scheme, a PP fault with different fault resistance is simulated in the DC cable between terminal 3 and 4. The mode-1 DC voltage measured at DC terminal 3 is shown in Fig. 4.5(a) for 10 Ω, 50 Ω and 100 Ω PPG fault resistance at a distance of 120 km from DC substation 3. As evident from Fig. 4.5(b),(c) and (d), TWAT for fault induced TW is 0.7006616660456 s, 0.7006616104826 s and 0.7006618401227 s for 10 Ω, 50 Ω and 100 Ω fault resistance induced TW for 500 kHz sampling frequency measurement, which is consistent and insensitive to fault resistance up to 100 Ω. Similarly, the AT for 10 Ω, 50 Ω and 100 Ω PP fault resistance induced TW is extracted for 50 kHz sampling frequency mode-1 voltage signal, derived from 500 kHz sampled signal using down sample and low pass filter blocks, and it is tabulated in Table 4.3. It is clear from Table 4.3 that the proposed TW based fault localization scheme estimates the fault location to be 119.41 km, 119.47 km and 119.24 km for the 10 Ω, 50 Ω and 100 Ω PP fault resistance respectively, which gives the FLE to be less than 0.38 % for fault resistance up to 100 Ω.

Table 4.3: Impact of fault resistance on proposed TW based fault localization scheme

Fault resistance (Ω)	AT of TW at DC terminal 3 (500 kHz), AT_1 (s)	AT of TW at DC terminal 3 (50 kHz), AT_2 (s)	($\|AT_1 - AT_2\|$) (μs)	Velocity Factor ($\mu s/km$)	CFL & AFL (km)	FLE (%)
10	0.7006616660456	0.70076496166304	103.29	0.865	120 & 119.41	0.295
50	0.7006616104826	0.70076500537326	103.34	0.865	120 & 119.47	0.265
100	0.7006618401227	0.70076496883253	103.12	0.865	120 & 119.24	0.38

4.4.3 Impact of measurement noise

The measurement noise in the voltage signals measured from EPTs can lead to inaccurate fault location estimation for DC faults. In this section, the effectiveness of proposed fault

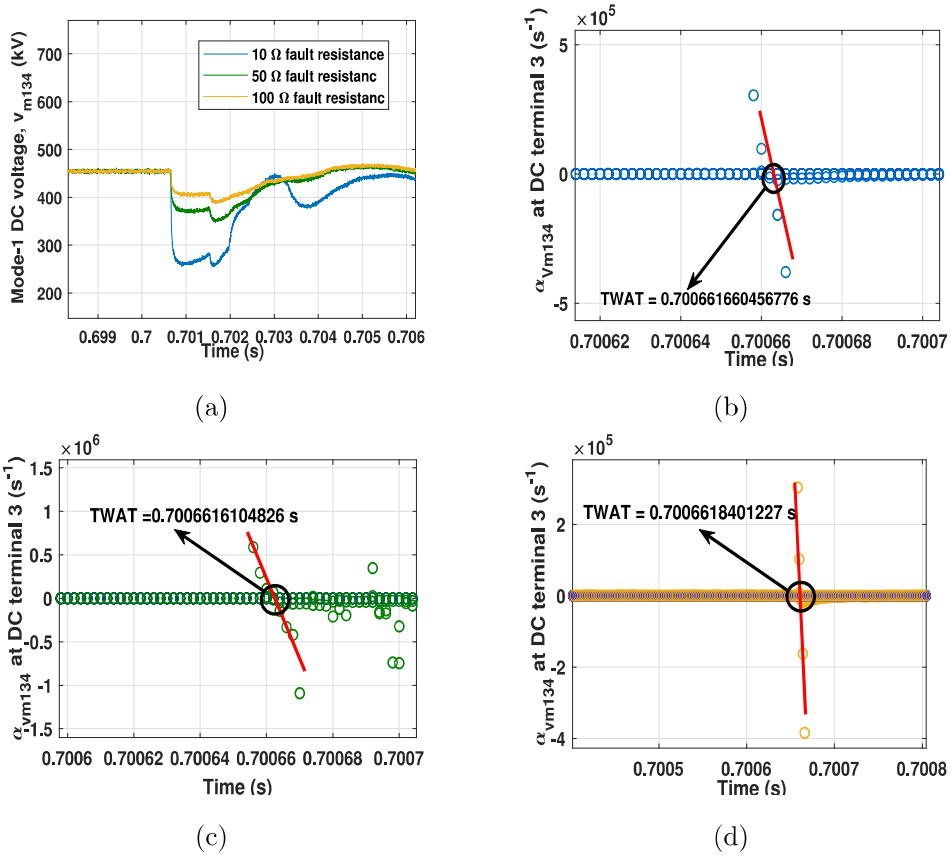

Figure 4.5: Impact of fault resistance on proposed TWAT estimation performance (a) Mode-1 DC voltage signal with 10 Ω, 50 Ω and 100 Ω PTG fault resistance at a distance of 120 km from DC substation 3, (b) AT estimation using proposed TWAT estimation technique for 10 Ω fault resistance, (c) AT estimation using proposed TWAT estimation technique for 50 Ω fault resistance, (d) AT estimation using proposed TWAT estimation technique for 100 Ω fault resistance.

localization scheme is evaluated against white Gaussian noise. Since the precision of fault localization approach hinges entirely on the accurate TWAT estimation of the fault-induced TW, it is essential to examine the accuracy of sliding MPM and linear regression technique's performance in the presence of noise interference for low sampling frequency (50 kHz) measurement. A pole-to-pole (PP) fault with 100 Ω fault resistance is simulated in DC cable between DC terminal 3 and 4 at a distance of 50 km from DC terminal 3. The measured mode-1 DC voltage at DC terminal 3 with no noise and with 40 dB signal-to-noise-ratio (SNR) is shown in Fig. 4.6 (a) and (b) respectively. The proposed sliding MPM and linear regression technique estimated the TWAT for measured mode-1 signal for both

scenarios to be 0.7003226152044 s and 0.7003225994183 s respectively as shown in 4.6 (c) and (d). The performance of proposed fault localization against noise contamination is further evaluated and tabulated in Tab 4.4, which concludes that the proposed fault localization scheme can efficiently estimates fault location for noise interference up to 40 dB SNR.

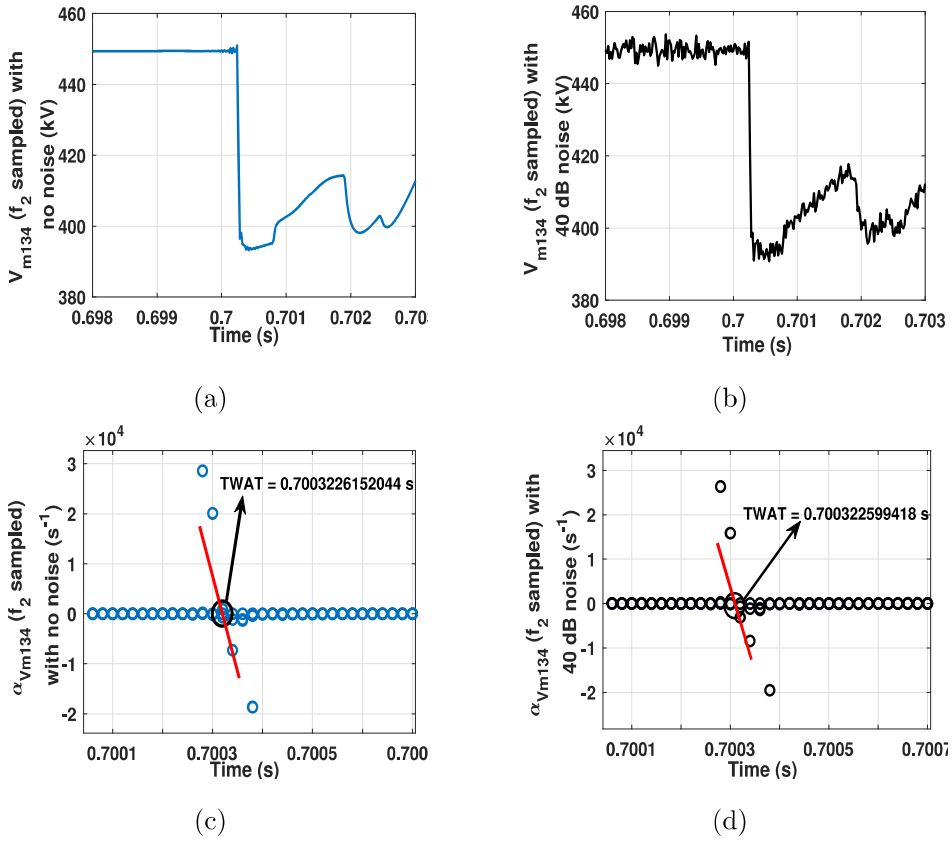

Figure 4.6: Impact of noise interference on proposed TWAT estimation performance (a) Mode-1 DC voltage without noise interference, (b) Mode-1 DC voltage voltage with 40 dB noise interference, (c) TWAT estimation for v_{m134} without noise interference, (d) TWAT estimation for v_{m134} with 40 dB noise interference.

4.4.4 Impact of fault type

To study the effect of fault types on the proposed single ended TW based fault localization scheme, PP fault, PPG and negative pole to ground (NPG) is simulated in DC cable $L34$ at a distance of 60 km from DC substation 3. The performance of proposed scheme is tabulated in Table 4.5, which confirms that accuracy of the proposed sliding MPM based

Table 4.4: Impact of noise on proposed TW based fault localization scheme

Noise (dB)	AT of TW at DC terminal 3 (500 kHz), AT_1 (s)	AT of TW at DC terminal 3 (50 kHz), AT_2 (s)	($\|AT_1 - AT_2\|$) (μs)	Velocity Factor ($\mu s/km$)	CFL & AFL (km)	FLE (%)
no noise	0.700279118492	0.7003226152044	43.4967	0.865	50 & 50.28	0.14
40	0.7002793821003	0.7003225994183	43.2173	0.865	50 & 49.96	0.02

Table 4.5: Impact of fault type on proposed TW based fault localization scheme

Fault Type (Ω)	AT of TW at DC terminal 3 (500 kHz), AT_1 (s)	AT of TW at DC terminal 3 (50 kHz), AT_2 (s)	($\|AT_1 - AT_2\|$) (μs)	Velocity Factor ($\mu s/km$)	CFL & AFL (km)	FLE (%)
PP	0.700335119386	0.70038728401	52.1	0.865	60 & 60.23	0.115
PPG	0.70033486002	0.70038693821	52.07	0.865	60 & 60.19	0.095
NPG	0.70033528401	0.70038752076	52.22	0.865	60 & 60.37	0.185

TWAT estimation technique is least affected by fault types in the MTDC grid. As evident for Table 4.5, the estimated fault location is 60.23 km, 60.19 km and 60.37 km for PP, PPG and NPG fault respectively. The FLE is found to be 0.115 %, 0.095 % and 0.185 % for PP, PPG and NPG fault respectively, which is very well within the allowed FLE range of 1 %.

4.4.5 Comparative analysis

To compare the performance of proposed sliding MPM based single ended TW fault localization scheme's performance against variational mode decomposition (VMD) based single ended TW fault localization scheme [131], a PPG and PP fault (10 Ω fault resistance) is simulated in DC cable L_{34} at 70 km distance from DC terminal 3 of MTDC grid described in Fig. 4.3. As evident from Fig. 4.7, the TWAT for 1^{st} and 2^{nd} TW at DC terminal is estimated using intrinsic mode function (IMF) of VMD, which comes out to be 0.700372 s and 0.701138 s. As per the conventional single ended TW based fault local-

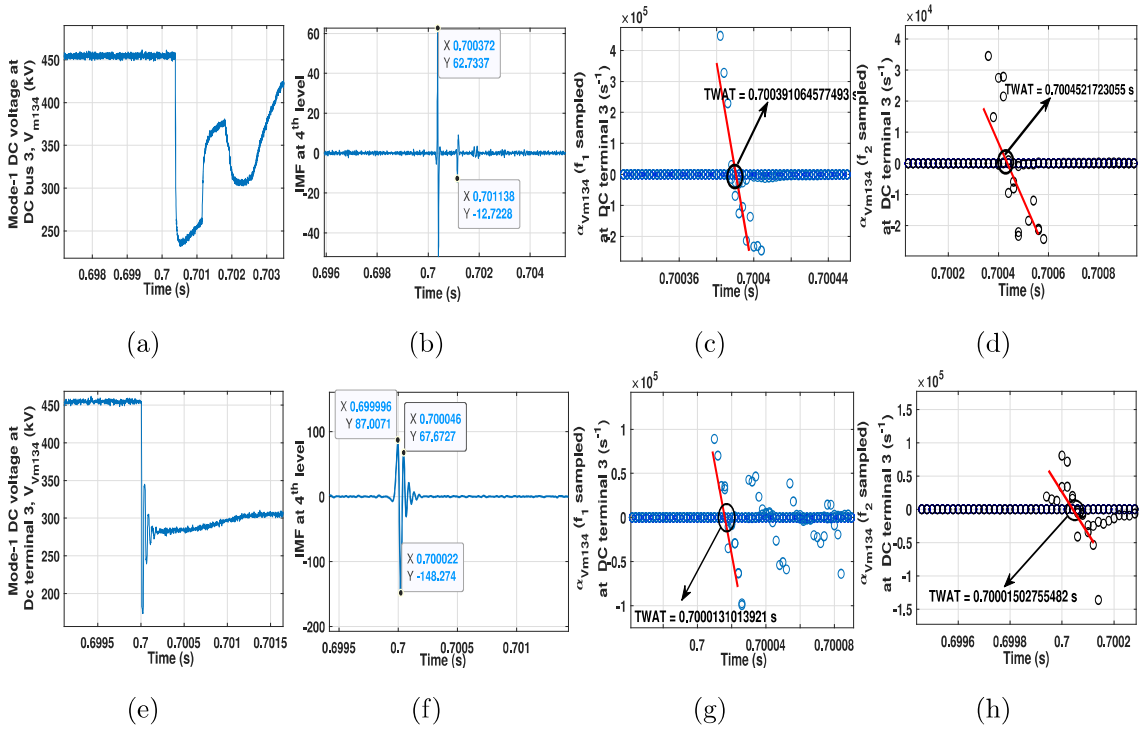

Figure 4.7: Comparative analysis (a) Mode-1 DC voltage at DC terminal 3 for fault at 70 km from DC substation 3, (b) IMF (4^{th} level) for mode-1 signal in (a), (c) TWAT for 1^{st} arrival TW for 500 kHz sampling frequency measured mode-1 DC voltage signal in (a), (d) TWAT for 1^{st} arrival TW for 50 kHz sampling frequency derived mode-1 DC voltage signal in (a), (e) Mode-1 DC voltage at DC terminal 3 for fault at 2 km distance from DC substation 3, (f) IMF (4^{th} level) for mode-1 signal in (e), (g) TWAT for 1^{st} arrival TW for 500 kHz sampling frequency measured mode-1 DC voltage signal in (e), (h) TWAT for 1^{st} arrival TW for 50 kHz sampling frequency derived mode-1 DC voltage signal in (e).

ization [131], the calculated fault location is 68.55 km. On the other hand, the proposed fault localization scheme estimates the TWAT as 0.7003910645775 s and 0.700452172306 s for the 500 kHz sampling frequency and 50 kHz (derived signal using downsample and low pass filter) respectively. As per 4.12 of the proposed fault localization scheme, the calculated fault location is 70.64 km. With comparative analysis, it can be inferred that the FLE of the proposed single ended TW based fault localization scheme (0.32 %) is lower than the conventional single ended TW based fault localization scheme (0.725 %) for lower sampling frequency (50 kHz) measurement.

The main limitation of the conventional TW based single ended fault localization scheme is its inability to locate fault closer to the DC terminal end, which is evident for the VMD based fault localization scheme's performance for the DC fault at 2 km from DC terminal as shown in Fig. 4.7(e). The IMF value (4^{th} level) for the mode-1 DC voltage level could not discriminate the first and second TWAT as shown in Fig. 4.7(e), therefore fails to locate DC fault. On the other hand, the proposed DC fault localization scheme detects TWAT as 0.7000131013921 s and 0.70001502755482 s for 500 kHz and 50 kHz sampling frequency measured mode-1 DC voltage signal. Using 4.12, the estimated fault location using proposed DC fault localization scheme is found to be 2.26 km and its associated FLE is 0.13 %, which helps to overcomes the limitation of conventional single ended TW based fault localization scheme.

4.5 Summary

This chapter proposes a traveling wave-based fault localization scheme, which only requires arrival instants of the first incident aerial mode traveling waves for high and derived low sampling frequency signal (using downsample and low pass filter component) at one line terminal of the MTDC grid. Therefore, the proposed scheme overcomes the challenging task of detecting reflected TW for close-in fault to the line terminal in a single ended TW based fault localization scheme. The proposed technique uses sliding MPM and linear regression tool to accurately estimate TWAT for high as well as low sampling frequency aerial mode signal, which assists in accurate fault localization. The effectiveness of proposed fault localization scheme is demonstrated against different fault resistance, fault location, fault type and noise interference. The sensitive analysis of proposed algorithm is also summarized here -

1. The maximum FLE for the proposed DC fault localization scheme is 0.55 % out of all fault location scenarios, except dead zone in the transmission line near DC terminal ends.

2. The proposed TWAT based fault localization technique can efficiently estimate fault location for fault impedance up to 100 Ω.

3. The proposed fault localization scheme can efficiently estimates fault location for

noise interference up to 40 dB SNR measurement noise conditions.

4. The proposed TW based fault localization scheme is less sensitive to different fault types. The FLE is found to be 0.115 %, 0.095 % and 0.185 % for PP, PPG and NPG fault respectively, which is very well within the allowed FLE range of 1 %/